

www.acsanm.org Article

Magnetic Fields and Magnetically Stimulated Gold-Coated Superparamagnetic Iron Oxide Nanoparticles Differentially Modulate L-Type Voltage-Gated Calcium Channel Activity in Midbrain Neurons

Muzhaozi Yuan, Eric A. Bancroft, Jingfan Chen, Rahul Srinivasan, and Ya Wang*



Cite This: ACS Appl. Nano Mater. 2022, 5, 205-215



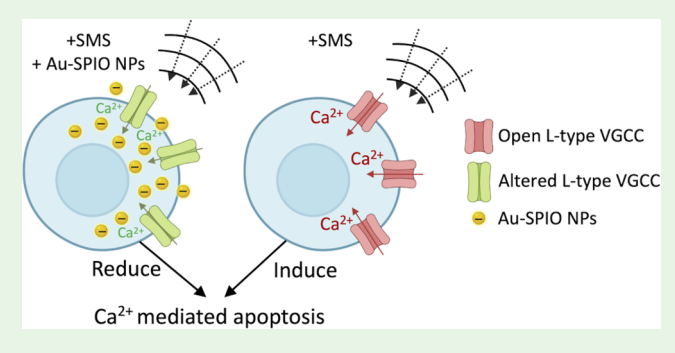
ACCESS

Metrics & More

Article Recommendations

Supporting Information

ABSTRACT: Nanoparticles (NPs) generate localized magnetic forces during magnetic stimulation, which can, in turn, modulate neuronal excitability and regulate downstream signaling in neurons. In agreement with this idea, under static magnetic field stimulation (SMS), gold-coated superparamagnetic iron oxide (Au-SPIO) core—shell nanoparticles (NPs) can promote and guide the direction of neurite outgrowth. Inspired by these promising results, this study investigates how SMS on Au-SPIO (SMS-Au-SPIO) affects the physiology of midbrain neurons. Transmission electron microscopy (TEM) images showed quasispherical shapes and a diameter of 20 ± 4 nm of Au-SPIO NPs synthesized by forming an Au layer on SPIO using a hydroxylamine hydrochloride-assisted



seed growth method. We found that SMS enhanced intracellular uptake of Au-SPIO and that SMS-Au-SPIO resulted in a delayed blockade of an L-type voltage-gated Ca²⁺ channel (VGCC) in midbrain neurons. Specifically, the frequency of spontaneous L-type VGCC-induced Ca²⁺ fluxes was significantly reduced in midbrain neurons exposed to either SMS or Au-SPIO or SMS-Au-SPIO. A power spectrum density analysis of Ca²⁺ fluxes showed that SMS decreased Ca²⁺ fluxes amplitudes (<0.1 Hz) before and after L-type VGCC blockade. By contrast, SMS-Au-SPIO decreased Ca²⁺ flux amplitudes only after L-type VGCC blockade, suggesting a modulation of L-type VGCC by SMS-Au-SPIO. Finally, while SMS alone induced apoptosis of dopaminergic (DA) neurons, SMS-Au-SPIO did not. Thus, SMS and SMS-Au-SPIO differentially modulate L-type VGCC-mediated Ca²⁺ fluxes, and downstream apoptotic signaling in midbrain neurons, implying the possible application of SMS-Au-SPIO as a drug delivery strategy to treat Parkinson's disease.

KEYWORDS: magnetically stimulated Au-SPIO nanoparticles, negative surface charge, midbrain DA neurons, L-type VGCC, calcium flux, apoptosis, Parkinson's disease

■ INTRODUCTION

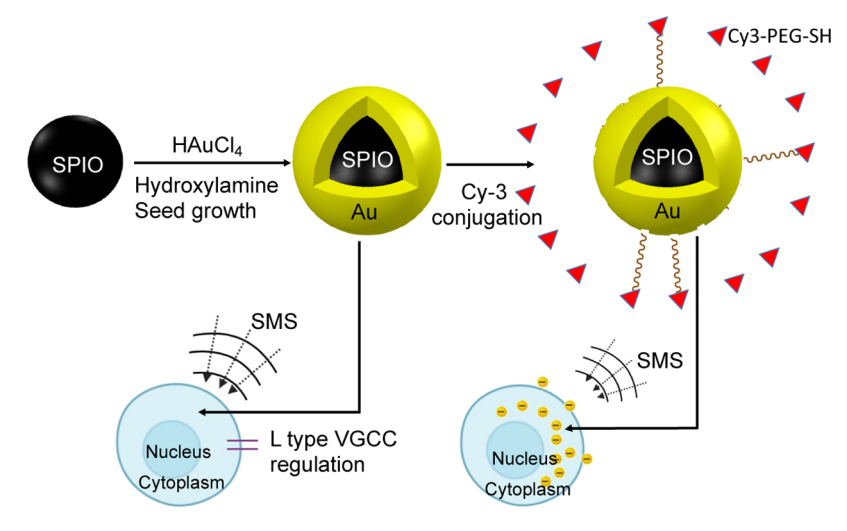
Parkinson's disease (PD) is the second most common neurodegenerative disease, characterized by a progressive loss of midbrain substantia nigra pars compacta (SNc) dopaminergic (DA) neurons.^{2,3} Unfortunately, current therapies for PD, such as treatment with levodopa or deep brain stimulation, are merely symptomatic and lose efficacy over time. As a consequence, novel strategies focused on regulating pacemaking activity in SNc DA neurons, thereby either slowing DA neuron loss or modulating basal ganglia circuitry, are an attractive therapeutic avenue for PD.5 Among these strategies, pulsed magnetic stimulation (MS) has gained attention as a noninvasive brain stimulation strategy. Pulsed MS promotes neuronal survival,6 stimulates neuronal differentiation,5,7 regulates intracellular Ca2+ flux,8 and induces membrane depolarization.9 However, off-target effects and poor localization of brain pulsed MS result in severe side effects such as epileptic seizures.¹⁰ In addition, interactions between magnetic fields and subcellular biological elements using MS alone may not be strong enough to selectively regulate neuronal activity.^{11,12} Static MS (SMS) has the potential to mitigate these side effects and can be combined with magnetic nanoparticles (NPs) to translate magnetic fields into highly localized mechanical forces at the cell membrane or within the cytoplasm.¹² In this regard, recent reports show that superparamagnetic iron oxide (SPIO) NPs under SMS can trigger Ca²⁺ fluxes by activating N-type mechanosensitive Ca²⁺

Received: August 26, 2021 Accepted: December 28, 2021 Published: January 5, 2022





Scheme 1. SPIO NPs Were Coated with Gold by the Seed Growth Process Using Hydroxylamine as Reducing Agent^a



^aOn one side, Au-SPIO NPs in combination with SMS were used to regulate L-type VGCC. On the other side, Au-SPIO NPs were functionalized with Cy3-PEG-SH as fluorescence dye to explore their interaction with midbrain DA neurons under the effect of SMS treatment.

channels in cortical neuron networks^{13,14} and opening mechanosensitive Ca²⁺ permeable ion channels (PIEZO2 and TRPV4) in primary dorsal root ganglion neurons.¹⁵

In this context, an unexplored question is whether or not SMS stimulation combined with SPIO NPs can affect the activity of L-type voltage-gated Ca2+ channels (VGCCs) in midbrain neurons, which is an important neuroprotective target for PD. 16 Since uncoated SPIO NPs with SMS stimulation may cause toxicity, 17,18 and are likely to aggregate, 19-21 we recently developed gold-coated SPIO (Au-SPIO) core-shell NPs, 22-25 which could improve the stability of SPIO NPs and protect them from reacting with biological media.^{26,27} We showed that Au-SPIO NPs displayed improved biocompatibility, cellular uptake and surface functionality, promoted growth and differentiation of neuronal PC-12 cells, 23,24 and facilitated targeted drug delivery. 28,29 Besides, Au-SPIO NPs with a size of 20 nm possess strong potential for efficient blood-brain barrier crossing. 30-35 It is also reported that Au NPs with similar size and surface parameters had a blood half-life of around 30 h and that the clearance of Au NPs occurs via the reticuloendothelial system in spleen and lymph nodes.³⁶ A prior study has shown that on attaching to the cell membrane, negative surface charges on NPs affect membrane polarization, thereby regulating VGCC activity.³⁷ In contrast, another study has reported that when compared to a negligible polarization effect of negative and neutral states, the uptake of positively charged Au NPs into cells causes membrane depolarization of different cell types, leading to an increase in Ca2+ flux.38 However, the effect of negatively charged Au-SPIO NPs on L-type VGCC-mediated Ca²⁺ fluxes in native midbrain neurons in the presence or absence of MS is completely unknown.

In this study, we prepared Au-SPIO NPs via a seed growth method using hydroxylamine hydrochloride as the reducing agent and modified the surface of Au-SPIO NPs by Cy3 fluorescence dye to explore their interaction with midbrain DA neurons (Scheme 1). We compared the effects of either SMS alone or SMS with Au-SPIO NPs (SMS-Au-SPIO) on Ca²⁺ activity in midbrain neurons. Using these Au-SPIO NPs, we showed that the exposure of cultured primary mouse midbrain neurons to either SMS through a Halbach array applicator or

SMS-Au-SPIO altered L-type VGCC-mediated spontaneous Ca²⁺ fluxes in midbrain neurons (Scheme 1). We suggest that this may be an important upstream event that explains the ability of SMS or SMS-Au-SPIO NPs to alter intracellular Ca²⁺ concentrations in midbrain neurons, thereby exerting neuroprotective effects in the preclinical animal models of PD.

EXPERIMENTAL SECTION

Preparation of Fluorescence-Tagged Au-SPIO NPs. Au-SPIO core-shell NPs were synthesized using the seed growth method according to our previously reported work.²³ First, SPIO core seeds were synthesized using a coprecipitation method²³ and synthesized SPIO seeds (60 mM) were diluted to 1.5 mM using deionized (DI) water. The diluted solution was mixed with sodium citrate (0.1 M) using an equal volume ratio (5.5 mL of SPIO: 5.5 mL of sodium citrate) and stirred for 10 min to allow for the exchange of OHabsorbed at the surface of SPIO seeds with citrate ligands. This solution was further diluted with 89 mL of DI water before adding 0.5 mL of HAuCl₄ solution (1%). The pH value of this solution was checked and adjusted between 8 and 10 using NaOH solution (0.1 M), followed by the addition of 0.6 mL of NH₂OH*HCl (0.2 M) into the solution to reduce Au³⁺ and form a Au shell at the surface of SPIO seeds within 5 min. This process was repeated by adding 0.5 mL of HAuCl₄ solution (1%) and 0.2 mL of NH₂OH*HCl (0.2 M) sequentially to form a thicker Au shell. The whole reaction was performed at room temperature. Synthesized Au-SPIO NPs were then separated using a magnet, washed three times with DI water, and finally dispersed in 7.5 mL of DI water. All of the chemicals used in this step were obtained from Sigma-Aldrich (St. Louis, MO).

To visualize an interaction between Au-SPIO NPs and midbrain neurons using confocal microscopy, it is necessary to use Cy3 dye for the fluorescence conjugation of Au-SPIO NPs, which do not autofluorescence. To do this, $\sim\!100~\mu\text{L}$ of Cy3-PEG-SH solution (PG2-S3TH-2k, Nanocs Inc.) at a concentration of 1 mg/mL was added to 1 mL of Au-SPIO solution at a concentration of 1.2747 mg/mL. After Cy3 conjugation, the resulting solution was mixed for 24 h, centrifuged, washed three times with DI water, and finally redispersed in 1 mL of DI water to remove the unbounded Cy3-PEG-SH.

Material Characterization. To reveal the morphology of Au-SPIO NPs, transmission electron microscopy (TEM) was performed using an FEI Tecnai G2 F20 S-Twin field-emission scanning transmission electron microscope (operating voltage: 200 kV). To confirm the existence of Au on SPIO, the light absorption spectrum was recorded at room temperature using a SHIMADZU UV-2450

ACS Applied Nano Materials

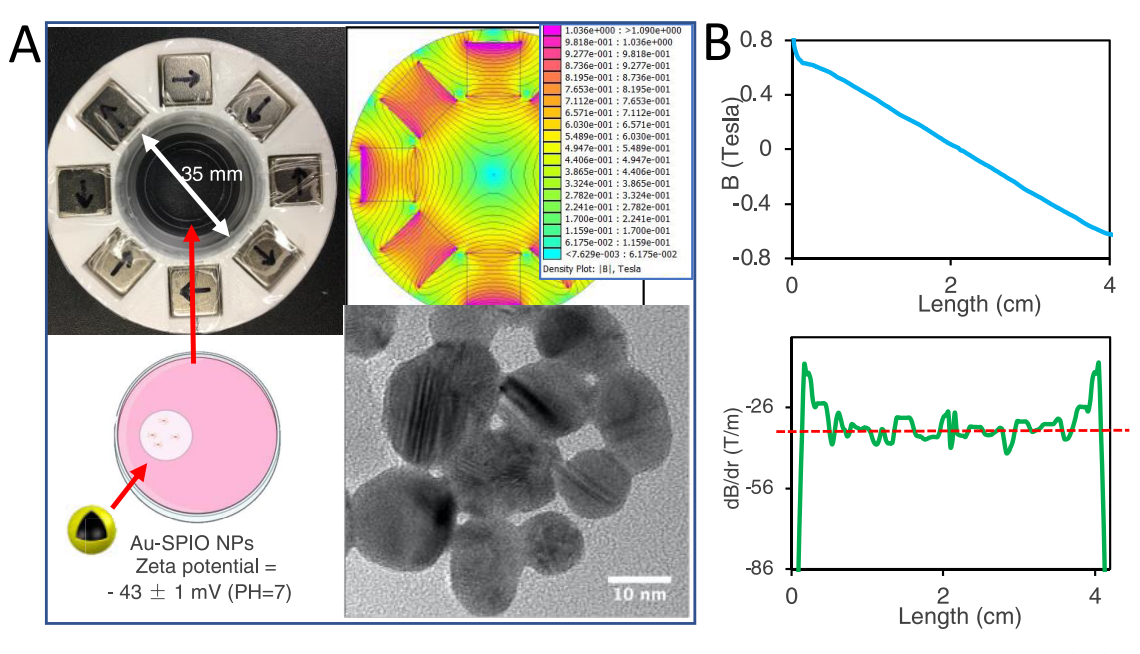


Figure 1. Properties of SMS and SMS-Au-SPIO treatment and their interaction with cultured DA neurons. (A) Top: the setup (left) and the finite element modeling (FEM) (right) of the static magnetic applicator using NS2 magnets; bottom: 35 mm Petri dish showing how cells in the coverslip (white circle) are positioned during SMS stimulation and the ζ-potential of Au-SPIO NPs as treatment in the cell culture medium (left); and a TEM image of Au-SPIO NPs (right). (B) Top: finite element modeling (FEM) result of the flux density inside the magnetic applicator and bottom: the gradient dB/dr (T/m) along the radial direction. The red dotted line indicates an estimated average value of dB/dr = -36.19 T/m.

spectrophotometer (Shimadzu Corp.) ζ -Potential and hydrodynamic diameter were measured by dynamic light scattering using a Zetasizer apparatus (Malvern Instruments). The results were obtained from triplicate experiments.

Culturing Primary Embryonic Mouse Midbrain Neurons. Reagents used to culture primary embryonic mouse DA neurons included neurobasal medium, DMEM + GlutaMAX medium, GlutaMAX supplement, B-27, equine serum, and penicillin—streptomycin purchased from ThermoFisher (Waltham, MA), as well as deoxyribonuclease I (DNase), poly-L-lysine, poly-L-ornithine, laminin, ascorbic acid, kanamycin, and ampicillin purchased from Sigma-Aldrich (St. Louis, MO). Papain was purchased from Worthington Biomedical Corporation (Lakewood, NJ). Corning 35 mm uncoated plastic cell culture dishes were purchased from VWR (Radnor, PA), and 12 mm circular cover glass No. 1 was purchased from Phenix Research Products (Candler, NC).

Detailed methods to culture primary embryonic mouse DA neurons have been previously described. $^{40-42}$ Briefly, cultures were obtained from embryonic day (ED14) mouse embryos of both sexes. Timed-pregnant mice (Texas A&M Institute for Genomic Medicine) were sacrificed by cervical dislocation and embryos were removed. Embryos were then decapitated, and the ventral midbrain was dissected using the methods previously described. 40-42 Cells were then digested in papain for 15 min at 37 °C. Next, cells were separated using DNase treatment and mechanical trituration in a stop solution of 10% equine serum in Hank's balanced salt solution (HBSS, Sigma-Aldrich). Cells were plated on a 12 mm cover glass triple coated with poly-L-lysine, poly-L-ornithine, and laminin at a density of 200 000 cells per cover glass. Following plating, cells were incubated at 37 °C with 5% CO2 for 1 h, followed by the addition of neurobasal media supplemented with GlutaMax, B-27, equine serum, ascorbic acid, and containing penicillin-streptomycin, kanamycin, and ampicillin. The culture medium was exchanged at 3 day intervals, and all primary cultures were allowed to mature for 3 weeks before experiments were performed. All experiments performed in this study were replicated on three to four independent midbrain cultures.

Adeno-Associated Viral (AAV) Vectors. To image spontaneous Ca²⁺ activity in primary midbrain neurons, we employed the adeno-associated virus AAV 2/5 hSyn-GCaMP6f purchased from Addgene (Cat #100837-AAV, RRID: Addgene_100837). AAV infections were

performed at 14 days *in vitro* (DIV), as previously described. Briefly, the culture medium was removed and 1 mL of serum-free DMEM + GlutaMAX medium containing 1 μ L of Syn-GCaMP6f (titer = 1 × 10¹³ genome copies/mL) was added to each dish and allowed to incubate at 37 °C with 5% CO₂ for 1 h. Next, the serum-free medium containing AAVs was removed and replaced with 3 mL of supplemented neurobasal medium. Imaging was performed 5 days following AAV infection.

Confocal Imaging of Spontaneous Ca2+ Fluxes in Cultured Midbrain Neurons. The protocol used for imaging spontaneous Ca²⁺ fluxes in primary midbrain neurons has been previously described.⁴ Briefly, cultures were placed in a gas-free recording buffer containing (mM): 154 NaCl, 5 KCl, 2 CaCl₂, 0.5 MgCl₂, 5 D-glucose, 10 HEPES, and pH adjusted to 7.4 with NaOH (all purchased from Sigma-Aldrich). Imaging was performed using a confocal microscope (Fluoview 1200, Olympus, Tokyo, Japan) with a 40×, 0.8 NA waterimmersion objective (Olympus). We used a 488 nm line of an argon laser to excite GCaMP6f. The imaging frame was clipped to allow for an image sampling rate of 1 frame per second (FPS). For all experiments, spontaneous Ca2+ was recorded for 300 s, and for L-type VGCC blocking experiments followed by 300 s of drug application. Ltype VGCCs were blocked using diltiazem (100 μ M), which has shown efficient and specific blocking of L-type VGCCs. 43-45 In the future, we will consider dihydropyridine drugs such as nifedipine as an alternative. Recording buffers were bath perfused using a peristaltic pump set at a rate of 2 mL/min. Diltiazem was purchased from Tocris (Minneapolis, MN). To quantify the exponential decay of blockade by diltiazem, Ca²⁺ traces were fitted to an exponential equation. Latency to blockade was determined for each condition by recording the time (in seconds) at which the last discernable (>0.1 $\Delta F/F_0$) Ca²⁴ event occurred for each neuron. Average latencies for each condition were then compared. For all imaging experiments, statistical tests and p values are reported in the figures and figure legends.

Immunostaining of Primary Midbrain Cultures. Immediately following imaging, cultures were placed in 10% formalin for 40 min. Cultures were permeabilized in 0.01% Triton X-100/phosphate-buffered saline (PBS) and blocked in 10% normal goat serum (NGS)/PBS solution. Antibodies used included chicken polyclonal antityrosine hydroxylase (TH) (1:1000, Abcam) and rabbit polyclonal anticleaved caspase-3 (1:1000, Cell Signaling Technologies, Danvers,

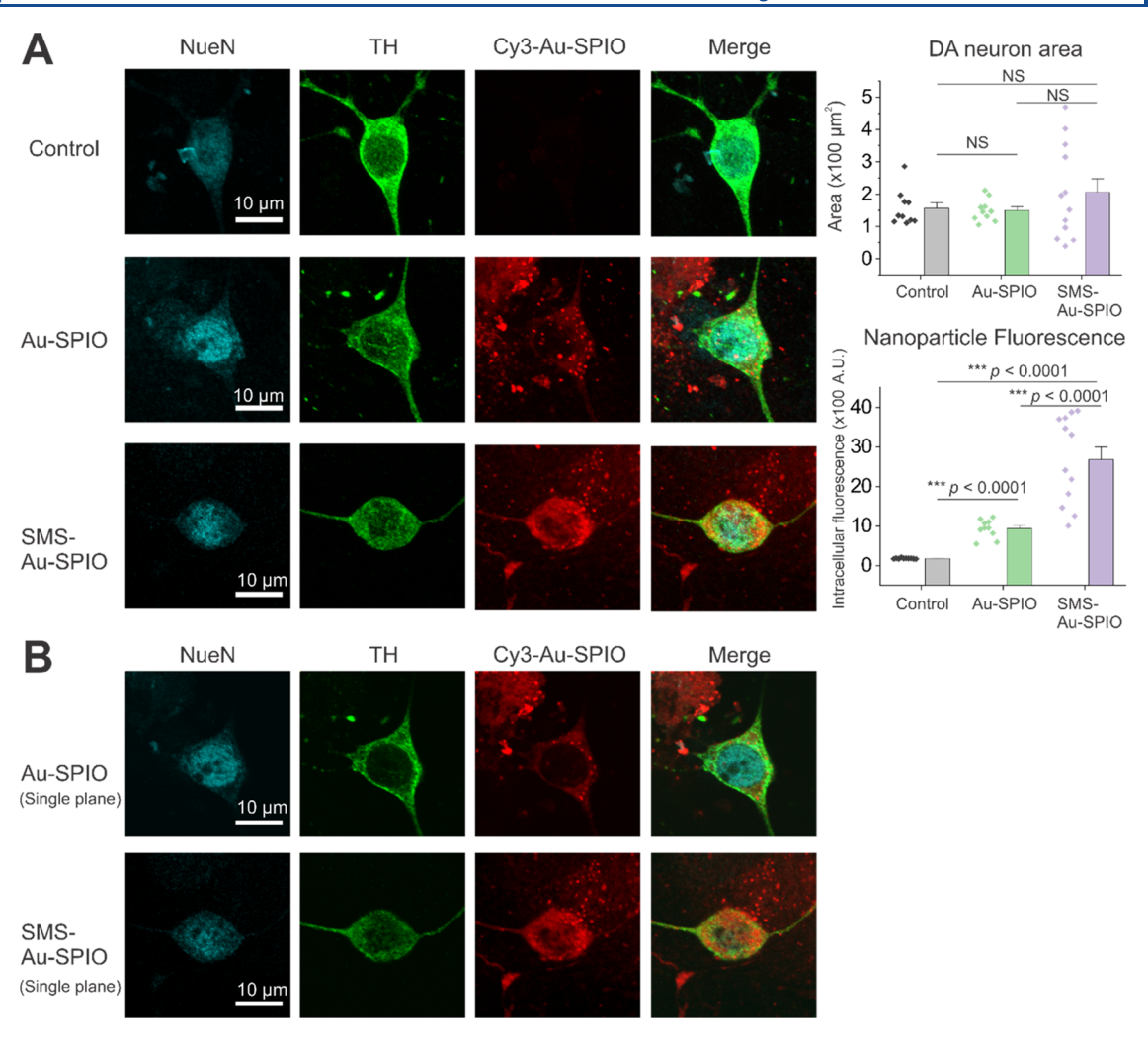


Figure 2. Interaction between SMS-Au-SPIO and cultured DA neurons. (A) Left: representative confocal z-stacks at $60 \times$ magnification of NeuN, TH, Cy3-tagged Au-SPIO expression, and merged images (NeuN, TH, and Cy3) in cultured primary midbrain neurons. Scale bar: $10 \mu m$. Right: summary data of DA neuron area and mean Cy3 fluorescence intensity. (B) Single optical plane images for Au-SPIO and SMS-Au-SPIO conditions from z-stacks in panel (A). Scale bar: $10 \mu m$. All experiments were performed on two independent cultures. n=10 control neurons, 10×10^{-5} neurons, and 10×10^{-5} Neurons. Error bars are \pm standard error of the mean (SEM) and p values are indicated for all graphs, based on two-sample t-test for normally distributed data and Mann–Whitney test for non-normally distributed data. p < 0.05 was considered statistically significant. NS = not significant.

MA). Imaging was performed using a confocal microscope (Fluoview 1200, Olympus) with a 60×, 1.35 NA oil-immersion objective (Olympus).

Evaluation of Power Spectral Density (PSD) for Spontaneous Ca^{2+} Flux Signals. The power spectral density (PSD) of a calcium flux signal x(t) can be expressed as the average of the Fourier transform magnitude squared over a large time interval.

$$S_x(f) = \lim_{T \to \infty} E\left\{ \frac{1}{2T} \left| \int_{-T}^{T} x(t) e^{-j2\pi f t} dt \right|^2 \right\}$$

In Matlab, a function called periodogram was used, which directly gave the results of PSD.

Evaluation of Synchronization of Spontaneous Ca²⁺ Fluxes Using Global Field Synchronization (GFS). Global field synchronization (GFS) can estimate the functional connectivity of brain processes. Here, we use this method to quantify the synchronization level of the neuron Ca²⁺ flux in a frequency-dependent manner. To determine GFS values, Ca²⁺ fluxes for each neuron recorded within individual fields of view were transformed into frequency domains using fast Fourier transform (FFT), which allows for comparison of Ca²⁺ flux amplitudes and phase at each frequency.⁴⁶ FFT-transformed signals at each frequency were then

visualized as a cloud of points in a complex plane, yielding two eigenvalues. GFS (0-1) was defined as 47

GFS(f) =
$$\frac{|E(f)_1 - E(f)_2|}{E(f)_1 + E(f)_2}$$

where $E(f)_1$ and $E(f)_2$ are two eigenvalues obtained from principal component analysis at a given frequency f. High GFS values in a given frequency indicate that a large part of the recorded calcium activity at that frequency is phase-locked, which can be interpreted as increased overall functional connectivity. Low GFS values indicate that no preferential phase could be determined. GFS = 1 indicates the complete synchronization of Ca^{2+} flux amplitudes and phase, while GFS = 0 indicates asynchronous Ca^{2+} fluxes. The Matlab code and functions for calculating the GFS value are given in the Supporting Information (SI).

■ RESULTS AND DISCUSSION

SMS Enhances the Intracellular Delivery of Au-SPIO NPs into Primary Cultured Mouse DA Neurons. Midbrain DA neurons were isolated from the ventral mesencephalon (VM) of mouse embryonic day 14 (E14) embryos and

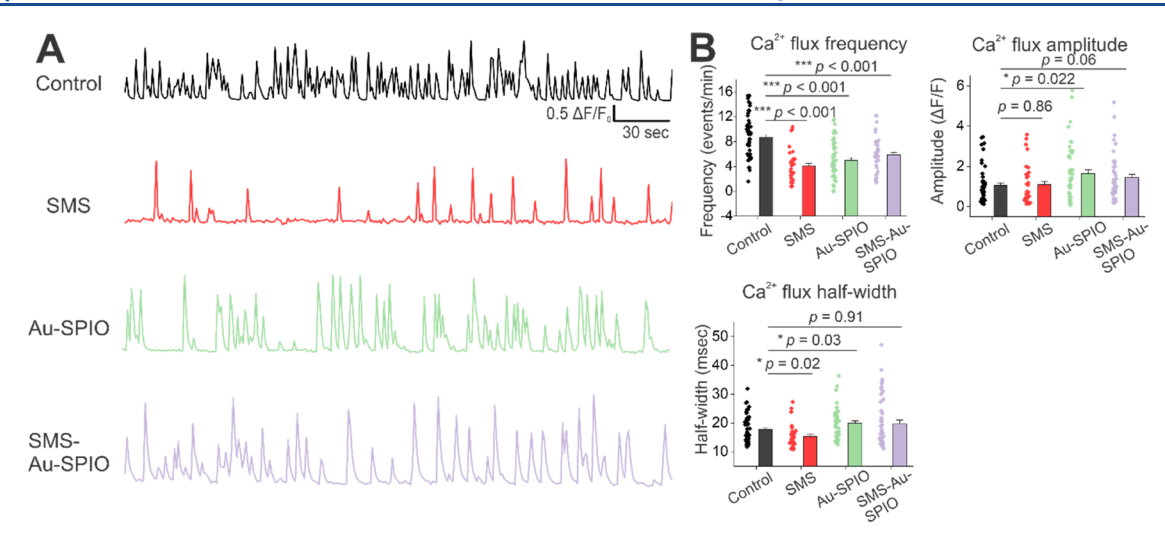


Figure 3. SMS and SMS-Au-SPIO alter spontaneous Ca^{2+} activity in cultured primary midbrain neurons. (A) Representative $\Delta F/F_0$ traces of spontaneous Ca^{2+} in primary midbrain neurons from each experimental condition. (B) Summary data of spontaneous Ca^{2+} flux frequency, amplitude, and half-width. All experiments were performed on four independent cultures. n = 50 control neurons, 33 SMS neurons, 50 Au-SPIO neurons, and 48 SMS-Au-SPIO neurons. Error bars are SEM and p values are reported in all graphs, based on Mann–Whitney tests for nonnormally distributed data or two-sample t-tests for normally distributed data. **General neuron vs. DA neuron**

mechanically dissociated. 40 Dissociated cells were further cultured for 2 weeks prior to treatment with 20 µg/mL of Au-SPIO NPs. To apply SMS, primary mouse midbrain cultures were placed inside a magnetic applicator composed of 8*N52 NdFeB magnetic cubes (0.5 in.) arranged in a Halbachlike array for 30 min (Figure 1A). Inside the applicator, a constant magnetic field gradient of -36.19 T/mwas estimated along the radial direction (Figure 1B). Au-SPIO NPs were synthesized using hydroxylamine hydrochloride to form an Au layer at the SPIO core according to a previously reported method.^{23,48} As shown in Figure 1A, the TEM images of Au-SPIO NPs displayed quasispherical shapes and an average diameter of 20 \pm 4 nm, while uncoated SPIO NPs displayed an average diameter of 13 ± 3 nm (Figure S1). The formation of a Au shell on SPIO was confirmed by a UV-vis light absorbance spectrum (Figure S2), which exhibited the characteristic light absorbance peak of Au shell at 523 nm. 22 ζ -Potential and hydrodynamic diameter results (Table S1) further showed that fresh Au-SPIO NPs possessed a negative ζ -potential of -44.2 ± 0.7 mV and a hydrodynamic diameter of 23.5 \pm 0.1 nm, while 1 month old Au-SPIO NPs had a negative ζ -potential of -42.3 ± 1.6 mV and a hydrodynamic diameter of 23.6 \pm 0.2 nm. The nearly unchanged ζ -potential and hydrodynamic diameter indicated their high stability in aqueous solution because of a strong electrostatic repulsive force. Our previous work also demonstrated no decrease of the characteristic absorbance peak for up to 21 days, suggesting that Au-SPIO NPs are stable in the cell culture medium. 22 It has been reported that Au coating affects the superparamagnetic property of SPIO and causes a slight reduction of magnetization from 59.6 to 54.3 emu/g.48 This can be attributed to the obstructed rotation of SPIO NPs by Au coating. To verify the magnetic properties of Au-SPIO NPs, we also tested their magnetic behavior using an external magnetic field. As shown in Figure S3, Au-SPIO NPs exhibited fast movement toward the magnetic field within 5 s, confirming the magnetic response of Au-SPIO NPs. To visualize interaction between Au-SPIO NPs and midbrain neurons using confocal microscopy, Au-SPIO NPs were tagged with Cy3 dye (Nanocs, cat #PG2-S3TH-2k, red), and midbrain neurons were stained

with antibodies against NeuN (Abcam, cat #ab104224) and tyrosine hydroxylase (TH) (Abcam, cat #ab76442). As shown with confocal z-stacks in Figure 2A, in the absence of SMS, a few negatively charged Au-SPIO NPs were internalized into the cytosol of midbrain neurons (average intracellular fluorescence = 932 AU), while SMS caused a significant increase in internalization of Au-SPIO NPs into midbrain neurons (average intracellular fluorescence = 2676 AU). To further demonstrate that Cy3-tagged Au-SPIO NPs were truly internalized into the neuronal cytosol, Figure 2B shows a single optical plane image of Au-SPIO and SMS-Au-SPIO from example cells in panel A. No significant difference was observed in the size of midbrain neurons between groups, suggesting that neither SMS nor Au-SPIO NPs caused osmotic swelling of neurons. Our previous work has demonstrated that Au-SPIO NPs can be absorbed by neuronlike cells through the endocytic pathway. 23,24 One of the possible mechanisms to enhance the internalization of Au-SPIO NPs into midbrain neurons via SMS is to promote endocytic uptake of NPs by overcoming the membrane deformation cost using SMS. 49 To further confirm this hypothesis, detailed experimental protocols can be designed to study different cellular uptake mechanisms, which will be explored in the future.

SMS-Au-SPIO Regulates Ca²⁺ Fluxes in Midbrain Neurons via L-Type VGCCs. A previous study has shown that negatively charged Au-SPIO NPs adhere to hippocampal neuronal membranes and modulate the excitability of these cells;³⁷ however, the underlying mechanisms are unclear. We therefore sought to determine differences in midbrain neuron activity following either exposure to Au-SPIO alone or coexposure to Au-SPIO with SMS. We rationalized that since SMS causes negatively charged Au-SPIO NPs to penetrate the cytoplasm of neurons (Figure 2), this will likely modulate spontaneous midbrain neuron Ca²⁺ fluxes in a manner that is distinct from exposure to Au-SPIO NPs without SMS.

To quantify spontaneous Ca²⁺ fluxes in cultured mouse midbrain neurons, we followed a previously published protocol.⁴⁰ Briefly, we used an AAV expressing the genetically encoded Ca²⁺ indicator, GCaMP6f, driven by a neuron-specific

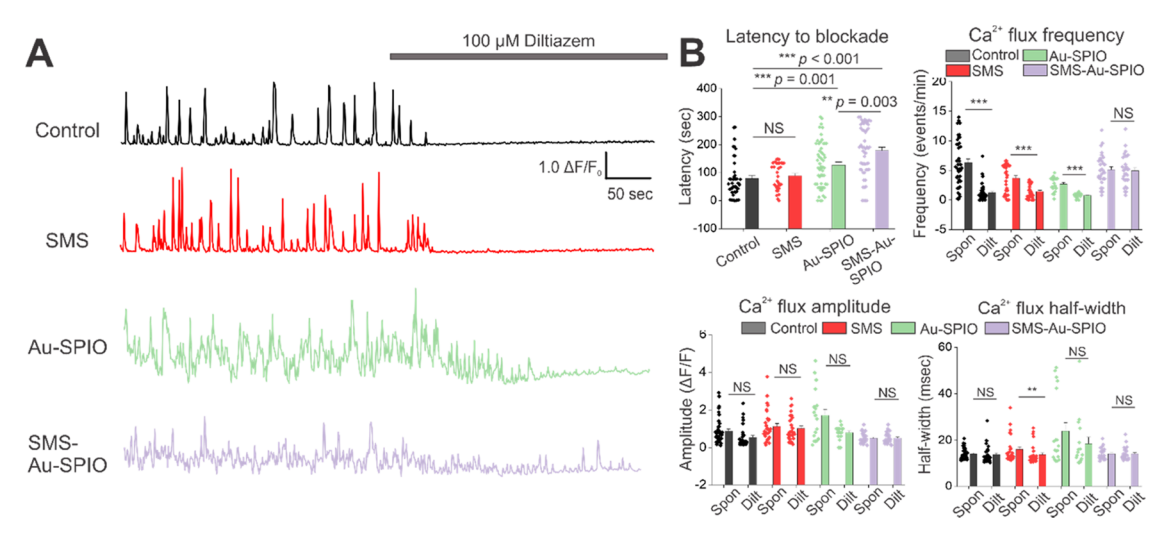


Figure 4. SMS and SMS-Au-SPIO alter Ca²⁺ activity via L-type VGCCs in cultured primary midbrain neurons. (A) Representative $\Delta F/F_0$ traces of primary midbrain neurons with L-type VGCC blocker diltiazem applied from 300 to 600 s following imaging of spontaneous events in the first 300 s as indicated by the gray bar. (B) Summary data including latency to L-type VGCC blockade, Ca²⁺ flux frequency, amplitude, and half-width prior to and during diltiazem application. All experiments were performed on three independent cultures. n = 46 control neurons, 33 SMS neurons, 57 Au-SPIO neurons, and 56 SMS-Au-SPIO neurons. Error bars are ± SEM and p values are indicated for all graphs, based on two-sample t-test for normally distributed data, Mann—Whitney test for non-normally distributed data, and paired-sample Wilcoxon-Sign rank test for paired measures. t < 0.05 is considered statistically significant. *t > 0.05, *t > 0.01, and *t > 0.001. NS = not significant.

human synapsin promoter (hSyn) (AAV 2/5 hSyn-GCaMP6f).

Two-week-old primary mouse midbrain neuron cultures were infected with 1×10^9 genome copies of AAV 2/5 hSyn-GCaMP6f per 35 mm dish and cultured for five additional days. Cells were then cultured for 24 h with exposure to 20 μ g/ mL Au-SPIO NPs. This concentration did not induce the toxicity of neuronlike cells in our previous study. 23,24 Before imaging, the cells were placed in the magnetic applicator for 30 min for both SMS and SMS-Au-SPIO groups. As shown in Figure 3A,B, in all cases, we observed robust spontaneous neuronal Ca2+ fluxes, but each treatment condition caused a distinct alteration in spontaneous Ca²⁺ flux activity. Specifically, when compared to untreated control cultures (average frequency = 8.7 events/min, average amplitude = 1.05 $\Delta F/F_0$, average half-width = 17.71 ms), SMS alone reduced the frequency (4.0 events/min) and half-width (15.36 ms) of Ca²⁺ fluxes, while Au-SPIO NPs alone reduced the frequency (4.9 events/min) but increased the amplitude (1.6 $\Delta F/F_0$) and half-width (19.96 ms) of Ca²⁺ fluxes. Coexposure to SMS-Au-SPIO reduced Ca²⁺ flux frequency (5.9 events/min) with no effect on half-width or amplitude.

We next asked if these spontaneous Ca^{2+} fluxes were caused by L-type VGCCs. Neuronal cultures were bath perfused with 100 μ M diltiazem, which is a specific inhibitor of L-type VGCCs. $^{43-45}$ Ca^{2+} fluxes in the presence of diltiazem were then imaged using a confocal microscope and analyzed. We first fit Ca^{2+} event traces following diltiazem exposure for each of the four conditions (Control, SMS, Au-SPIO, SMS-Au-SPIO) to exponential fits. We found that SMS, Au-SPIO, and SMS-Au-SPIO decreased decay rates by approximately 40% when compared to untreated control cells (Figure S4). Having found a substantial difference in decay rates with each of the three manipulations, we then analyzed latency to complete blockade by diltiazem as reported in the Experimental Section.

As shown in Figure 4A,B, diltiazem almost completely inhibited spontaneous Ca^{2+} fluxes in untreated control cultures (spontaneous = 6.3 events/min, diltiazem = 1.2 events/min), suggesting that the spontaneous Ca^{2+} fluxes in these midbrain

neurons were predominantly caused by L-type VGCCs. Interestingly, when compared to control (78.7 s), the blockade by diltiazem was significantly delayed by both Au-SPIO NPs (127.1 s) and SMS-Au-SPIO (178.8 s) but not with SMS (88.8 s) exposure alone. One mechanism that could contribute to delayed blockade by diltiazem is a change in the activity of Ltype VGCCs due to changes in the resting membrane potential of midbrain neurons, caused by negatively charged Au-SPIO NPs. Interestingly, SMS did not alter the amplitude but altered the frequency of Ca²⁺ fluxes. The effect of SMS on ion channel properties and voltage gating are complex and difficult to interpret per se. The observed absence of delay following Ltype VGCC blockade, despite changes in Ca²⁺ flux frequency, could be explained by the idea that channel open times are regulated distinctly from voltage sensing and desensitization. Indeed, a recent study has shown that magnetic fields alter the kinetics of voltage-gated sodium and potassium channels via possible effect on sialic acid glycosylation motifs on these channels.⁵⁰ This suggests that the mechanism of voltage sensing is dependent on SMS, while the influx of ions through VGCCs is regulated by mechanisms that do not depend on SMS. Additionally, in our recent work,⁵¹ we have proved that the activity of L-type VGCC in DA neurons did not depend on the calcium release from the endoplasmic reticulum. We have also shown that the activity of L-type VGCC mainly depends on the extracellular Ca²⁺ level rather than the intracellular Ca²⁺

Note that Figure 4A contains representative $\Delta F/F_0$ Ca²⁺ traces for each condition, including a gray bar labeled "100 μ M Diltiazem" to denote when diltiazem was added. In Figure 4B, for graphs representing population data, each dot for each condition represents the value of a single cell. The wide distribution of data for each condition is because of inherent variability that is observed in native cocultures of astrocytemidbrain neurons. ^{40,41}

To gain more insight into how the activity of L-type VGCCs was altered by different treatment conditions, we utilized FFT as a method to transform the Ca²⁺ flux from the time domain

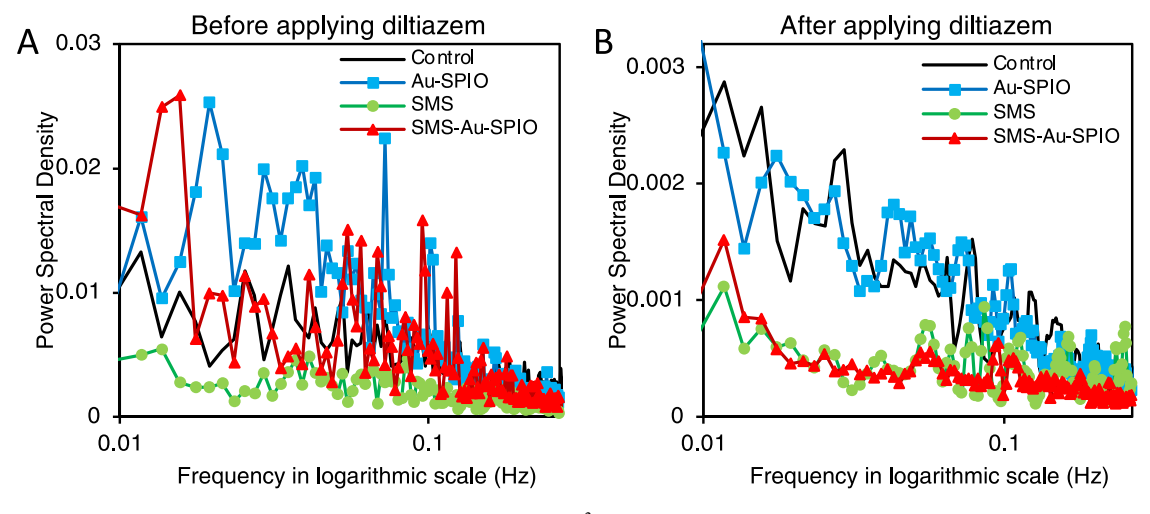


Figure 5. Differential effects of SMS and SMS-Au-SPIO on regulating Ca^{2+} flux amplitudes gated by L-type VGCC at lower frequencies <0.1 Hz. The PSD of spontaneous Ca^{2+} flux (A) before and (B) after the diltiazem application.

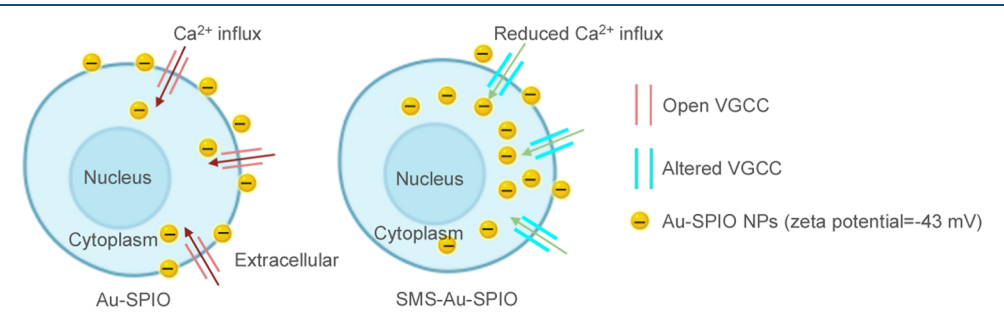


Figure 6. Schematic illustration of SMS-Au-SPIO regulating L-type VGCC activity.

to the frequency domain. We then obtained the PSD for Ca²⁺ fluxes in each midbrain neuron. Thus, PSD would reflect changes in the amplitude of the Ca²⁺ fluxes at each discreet frequency. We analyzed the PSD of spontaneous Ca²⁺ fluxes before (Figure 5A) and after (Figure 5B) diltiazem application. As shown in Figure 5A, PSD analysis of untreated control cultures showed that there were significant differences in Ca²⁺ flux amplitude within the lower range of frequencies (<0.1 Hz, corresponding to 0.6-6 events/min). Compared to controls, SMS decreased while Au-SPIO NPs increased Ca²⁺ flux amplitudes at lower frequencies <0.1 Hz. Interestingly, SMS-Au-SPIO did not affect Ca^{2+} flux amplitude at lower frequencies; however, after diltiazem application (Figure 5B), both SMS and SMS-Au-SPIO decreased the amplitude of Ca²⁺ fluxes. In addition, Au-SPIO alone did not affect the amplitude of Ca²⁺ fluxes in midbrain neurons. These data confirm that SMS-Au-SPIO regulates L-type VGCC activity, but the underlying mechanism is unclear. One possibility is that the Au-SPIO NPs without SMS are adhered to the extracellular surface of the neuronal plasma membrane, as shown in Figure 2. This can modulate membrane potential and alter spontaneous Ca²⁺ fluxes (Figure 6).³⁷ However, since SMS causes internalization of negatively charged Au-SPIO NPs into the cytosol of midbrain neurons (Figure 2), this would also alter membrane potential and delay the diltiazem-mediated blockade of Ca²⁺ activity (Figure 6). This hypothesis is based on our recent observation that SMS-Au-SPIO NPs hyperpolarize the membrane potential of PC-12 cells, while Au-SPIO NPs alone depolarize the membrane potential of PC-12 cells, 52 which is possibly due to the cellular mobility change of Au-SPIO NPs under SMS. Importantly, PC-12 cells possess

several properties that are similar to midbrain DA neurons, including the expression of tyrosine hydroxylase and the synthesis of dopamine. Therefore, we believe that Au-SPIO NPs in the presence of SMS will similarly cause a hyperpolarization of the resting membrane potential and membrane resistance of DA neurons.

It is interesting to note that although SMS alone reduced the excitability of neurons in lower frequencies (<0.1 Hz), SMS did not affect the latency to diltiazem-mediated L-type VGCC blockade. Since the lower frequencies of Ca^{2+} activity would correspond to a sparse population of active VGCCs in a neuron, this would allow SMS to manipulate the amplitude of VGCC-mediated Ca^{2+} influx more efficiently. Future study will be performed to further explore how SMS-Au-SPIO affects the change in the membrane resistance of midbrain DA neurons.

SMS-Au-SPIO Alters Midbrain Neuron Synchronization. As midbrain neurons establish synapses via axonal growth, ⁵⁴ synchronous neuronal Ca²⁺ fluxes between them play an important role in regulating these processes. 55-58 Excessive synchronization of electroencephalography signals has been observed in PD patients between their motor cortex and basal ganglia.⁵⁹ However, it is unclear if neighboring DA neuron synchronization in the midbrain is associated with PD pathology and how this is related with L-type VGCC activity. Based on these studies, we sought to determine the extent to which SMS-Au-SPIO NPs can modulate the synchronization of Ca2+ fluxes in midbrain neurons. To do this, we first conducted a synchronization analysis of neighboring midbrain neurons using GFS to quantify multiple Ca2+ fluxes in an interdependent single system from the large sets of midbrain neurons. GFS is more efficient and accurate 46,60 in comparison

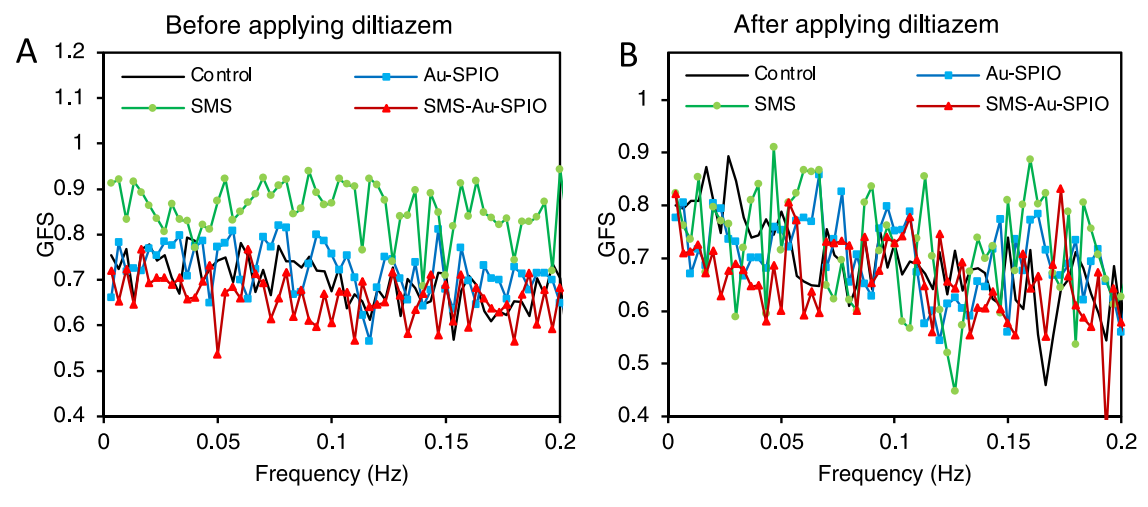


Figure 7. Effect of SMS and SMS-SPIO-Au on the synchronicity of Ca^{2+} fluxes in midbrain neurons before and after diltiazem application. GFS value (A) before and (B) after diltiazem application. A GFS value between 0 and 1 reflects the level of synchronization of Ca^{2+} fluxes between two neurons, where GFS = 1 indicates the full synchronization of Ca^{2+} fluxes and GFS = 0 indicates no synchronization.

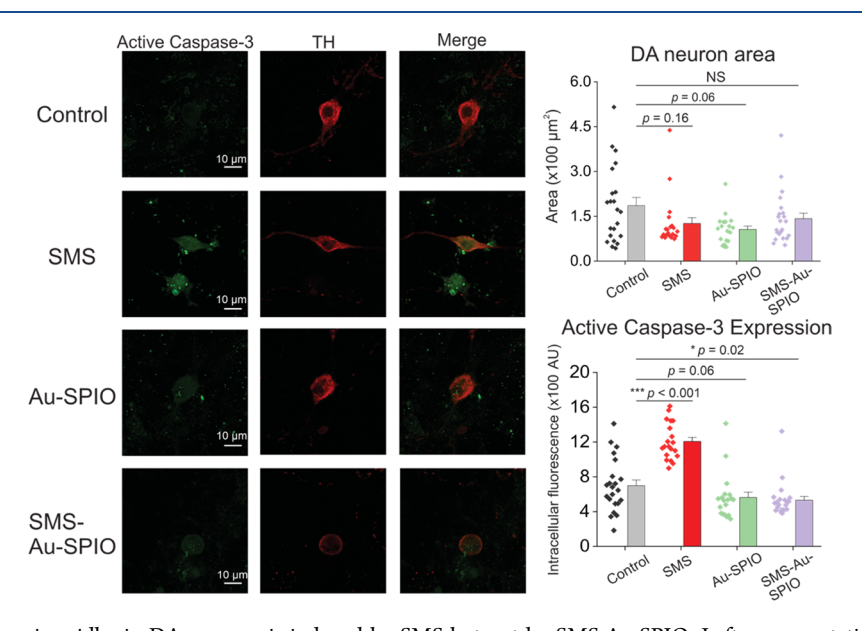


Figure 8. Caspase-3 cleavage in midbrain DA neurons is induced by SMS but not by SMS-Au-SPIO. Left: representative confocal images at $60 \times$ magnification of cleaved caspase-3 and TH expression (DA neuron marker) in cultured primary midbrain neurons. Scale bar: $10 \ \mu m$. Right: summary data of DA neuron area (top) and active caspase-3 expression (bottom). All experiments were performed on three independent cultures. n=22 control neurons, 20 SMS neurons, 19 Au-SPIO neurons, and 29 SMS-Au-SPIO neurons. Error bars are \pm SEM. p values are indicated for all graphs and are based on two-sample t-test for normally distributed data and Mann—Whitney test for non-normally distributed data. p < 0.05 is considered statistically significant. NS = not significant.

to the conventional approach,⁵⁵ which is mainly done manually by counting the percentage of cells that display simultaneous Ca²⁺ fluxes (GFS = 1 indicates the complete synchronization of Ca²⁺ flux amplitudes and phase, while GFS = 0 indicates asynchronous Ca²⁺ fluxes.). GFS analysis of all three groups (SMS, Au-SPIO, and SMS-Au-SPIO) showed that before applying diltiazem, SMS-Au-SPIO and Au-SPIO did not affect synchronization, while SMS slightly increased synchronization (Figure 7A). Additional postdiltiazem experiments showed that all three groups maintained similar synchronicity as untreated control cells (Figure 7B). These data suggest that the SMS-induced Ca²⁺ synchronization is mainly gated by L-type VGCC in midbrain neurons, and such an effect can be reversed by adding Au-SPIO NPs.

SMS-Au-SPIO Does Not Induce DA Neuron Apoptosis in Cultured Mouse Midbrain Neurons. Since dysregulated Ca²⁺ fluxes play an important role in the pathogenesis of neurodegeneration in PD, we sought to determine the effect of SMS and SMS-Au-SPIO NPs on apoptotic signaling in cultured DA neurons. For this purpose, we used TH as a DA neuron marker and an antibody against cleaved caspase-3 (cell signaling, cat #9661S) as a marker for apoptosis. We found that, when compared to control (699.4 AU), SMS (1206.1 AU) alone significantly increased while SMS-Au-SPIO (530.9 AU) decreased the levels of cleaved caspase-3 in DA neurons. In addition, Au-SPIO (563.3 AU) alone did not result in an obvious increase in cleaved caspase-3 (Figure 8). Taken together with the synchronization results, these findings suggest that SMS likely induces caspase-3 activation and

initiates apoptosis by increasing the synchronization of neuronal Ca^{2^+} fluxes. Furthermore, it is likely that the addition of Au-SPIO interrupts the mechanism by which SMS increases Ca^{2^+} flux synchronicity, consequently preventing caspase-3 activation and apoptosis.

CONCLUSIONS

In summary, we demonstrate that SMS and SMS-Au-SPIO can regulate spontaneous Ca2+ fluxes in midbrain neurons via the modulation of L-type VGCC activity. We first explored the interaction between Au-SPIO and DA neurons and found that SMS could significantly enhance the intracellular delivery of negatively charged Au-SPIO NPs to DA neurons. We then revealed a significant reduction in the frequency of spontaneous Ca2+ fluxes in midbrain neurons exposed to SMS, Au-SPIO, or the combination of SMS-Au-SPIO, suggesting that SMS and Au-SPIO when used in combination or alone are capable of regulating spontaneous Ca²⁺ fluxes in midbrain neurons. The delayed L-type VGCC blockade by SMS-Au-SPIO suggests that SMS-Au-SPIO treatment modulates Ca²⁺ fluxes by altering the L-type VGCC activity, which is further demonstrated by PSD calculation. GFS analysis and an evaluation of apoptosis with cleaved caspase-3 suggest that SMS-induced synchronization of Ca²⁺ flux may initiate apoptosis while combining SMS with Au-SPIO NPs reduces the apoptosis. Taken together, these results suggest that combining SMS with Au-SPIO NPs may be an effective neuroprotective strategy for PD. They further suggest that neuroprotection by SMS-Au-SPIOs likely occurs via a regulation of L-type VGCC activity and consequent attenuation of apoptotic signaling cascades. SMS-Au-SPIO could also serve as a potential tool for targeted delivery of therapeutic agents to specific brain regions and the localized modulation of Ca²⁺ flux activity. These results also provide important insights into how SMS-Au-SPIO modulates spontaneous Ca²⁺ fluxes and the associated downstream cellular processes in midbrain neurons. Future studies will explore the effect of NP surface charge, pH, and other parameters on the cellular uptake of NPs, as well as their ability to electrically tune the activity of native midbrain neurons with and without SMS. The additional experiments will be performed to explore how long it takes to reach the maximum accumulation of Au-SPIO in DA neurons. We will also dissect the relationship between L-type VGCC activity, Ca2+ flux synchronization, and apoptotic signaling. In future studies, in vivo experiments will be performed to verify toxicity, biodistribution, and pharmacokinetic behavior of SMS-Au-SPIO, as well as the targeted delivery of therapeutic agents to specific brain regions. We will also explore if SMS-Au-SPIO-induced alterations in spontaneous Ca²⁺ activity affect dopamine release and thus PD therapeutics.

ASSOCIATED CONTENT

5 Supporting Information

The Supporting Information is available free of charge at https://pubs.acs.org/doi/10.1021/acsanm.1c02665.

SMS triggering synchronized Ca²⁺ flux (AVI)

Matlab code and functions for calculating the GFS value and the UV-vis absorption spectra of SPIO-Au NPs (PDF)

AUTHOR INFORMATION

Corresponding Authors

Rahul Srinivasan — Department of Neuroscience & Experimental Therapeutics, College of Medicine, Texas A&M University, Bryan, Texas 77807-3260, United States; Texas A&M Institute for Neuroscience (TAMIN), Texas A&M University, College Station, Texas 77843, United States; orcid.org/0000-0003-0237-6602; Email: rahul@tamu.edu

Ya Wang — J. Mike Walker '66 Department of Mechanical Engineering, Texas A&M University, College Station, Texas 77840, United States; Department of Biomedical Engineering, Texas A&M University, College Station, Texas 77843, United States; Department of Electrical and Computer Engineering, Texas A&M University, College Station, Texas 77843, United States; Email: ya.wang@ tamu.edu

Authors

Muzhaozi Yuan – J. Mike Walker '66 Department of Mechanical Engineering, Texas A&M University, College Station, Texas 77840, United States; orcid.org/0000-0001-5542-065X

Eric A. Bancroft – Department of Neuroscience & Experimental Therapeutics, College of Medicine, Texas A&M University, Bryan, Texas 77807-3260, United States

Jingfan Chen – J. Mike Walker '66 Department of Mechanical Engineering, Texas A&M University, College Station, Texas 77840, United States

Complete contact information is available at: https://pubs.acs.org/10.1021/acsanm.1c02665

Author Contributions

*M.Y. and E.A.B. contributed equally to this work. The manuscript was written through the contributions of all authors. All authors have given approval to the final version of the manuscript.

Notes

The authors declare no competing financial interest.

ACKNOWLEDGMENTS

This work was supported by the NSF CAREER (grant number 1751435, Y.W.), NSF GCR (grant number 2021081, Y.W. and R.S), and by NIH NINDS (grant number RO1 NS115809, R.S.).

■ REFERENCES

- (1) Surmeier, D. J.; Schumacker, P. T.; Guzman, J. D.; Ilijic, E.; Yang, B.; Zampese, E. Calcium and Parkinson's disease. *Biochem. Biophys. Res. Commun.* **2017**, 483, 1013–1019.
- (2) Surmeier, D. J.; Guzman, J. N.; Sanchez-Padilla, J.; Schumacker, P. T. The role of calcium and mitochondrial oxidant stress in the loss of substantia nigra pars compacta dopaminergic neurons in Parkinson's disease. *Neuroscience* **2011**, *198*, 221–231.
- (3) Surmeier, D. J. Calcium, ageing, and neuronal vulnerability in Parkinson's disease. *Lancet Neurol.* **2007**, *6*, 933–938.
- (4) Mead, B. P.; Kim, N.; Miller, G. W.; Hodges, D.; Mastorakos, P.; Klibanov, A. L.; Mandell, J. W.; Hirsh, J.; Suk, J. S.; Hanes, J.; et al. Novel focused ultrasound gene therapy approach noninvasively restores dopaminergic neuron function in a rat Parkinson's disease model. *Nano Lett.* **2017**, *17*, 3533–3542.
- (5) Cantello, R.; Tarletti, R.; Civardi, C. Transcranial magnetic stimulation and Parkinson's disease. *Brain Res. Rev.* **2002**, *38*, 309–327.

- (6) Oda, T.; Koike, T. Magnetic field exposure saves rat cerebellar granule neurons from apoptosis in vitro. *Neurosci. Lett.* **2004**, *365*, 83–86
- (7) Chervyakov, A. V.; Chernyavsky, A. Y.; Sinitsyn, D. O.; Piradov, M. A. Possible mechanisms underlying the therapeutic effects of transcranial magnetic stimulation. *Front. Hum. Neurosci.* **2015**, *9*, No. 303.
- (8) Li, Y.; Yan, X.; Liu, J.; Li, L.; Hu, X.; Sun, H.; Tian, J. Pulsed electromagnetic field enhances brain-derived neurotrophic factor expression through L-type voltage-gated calcium channel-and Erk-dependent signaling pathways in neonatal rat dorsal root ganglion neurons. *Neurochem. Int.* **2014**, 75, 96–104.
- (9) Ma, J.; Zhang, Z.; Su, Y.; Kang, L.; Geng, D.; Wang, Y.; Luan, F.; Wang, M.; Cui, H. Magnetic stimulation modulates structural synaptic plasticity and regulates BDNF–TrkB signal pathway in cultured hippocampal neurons. *Neurochem. Int.* **2013**, *62*, 84–91.
- (10) Durmaz, O.; Mehmet Alpay, A.; Şenol, M. G. Repetitive transcranial magnetic stimulation (rTMS)-induced trigeminal autonomic cephalalgia. *Arch. Neuropsychiatry* **2015**, *52*, No. 309.
- (11) Wang, N.; Butler, J. P.; Ingber, D. E. Mechanotransduction across the cell surface and through the cytoskeleton. *Science* **1993**, 260, 1124–1127.
- (12) Hughes, S.; McBain, S.; Dobson, J.; El Haj, A. J. Selective activation of mechanosensitive ion channels using magnetic particles. *J. R. Soc. Interface* **2008**, *5*, 855–863.
- (13) Tay, A.; Kunze, A.; Murray, C.; Di Carlo, D. Induction of calcium influx in cortical neural networks by nanomagnetic forces. *ACS Nano* **2016**, *10*, 2331–2341.
- (14) Tay, A.; Di Carlo, D. Magnetic nanoparticle-based mechanical stimulation for restoration of mechano-sensitive ion channel equilibrium in neural networks. *Nano Lett.* **2017**, *17*, 886–892.
- (15) Tay, A.; Sohrabi, A.; Poole, K.; Seidlits, S.; Di Carlo, D. A 3D magnetic hyaluronic acid hydrogel for magnetomechanical neuromodulation of primary dorsal root ganglion neurons. *Adv. Mater.* **2018**, *30*, No. 1800927.
- (16) Ortner, N. J. Voltage-Gated Ca²⁺ Channels in Dopaminergic Substantia Nigra Neurons: Therapeutic Targets for Neuroprotection in Parkinson's Disease? *Front. Synaptic Neurosci.* **2021**, *13*, No. 5.
- (17) Mahmoudi, M.; Hofmann, H.; Rothen-Rutishauser, B.; Petri-Fink, A. Assessing the in vitro and in vivo toxicity of superparamagnetic iron oxide nanoparticles. *Chem. Rev.* **2012**, *112*, 2323–2338
- (18) Yarjanli, Z.; Ghaedi, K.; Esmaeili, A.; Rahgozar, S.; Zarrabi, A. Iron oxide nanoparticles may damage to the neural tissue through iron accumulation, oxidative stress, and protein aggregation. *BMC Neurosci.* **2017**, *18*, No. 51.
- (19) Cheng, Y.; Morshed, R. A.; Auffinger, B.; Tobias, A. L.; Lesniak, M. S. Multifunctional nanoparticles for brain tumor imaging and therapy. *Adv. Drug Delivery Rev.* **2014**, *66*, 42–57.
- (20) Nam, S. Y.; Ricles, L. M.; Suggs, L. J.; Emelianov, S. Y. Imaging strategies for tissue engineering applications. *Tissue Eng., Part B* **2015**, 21, 88–102.
- (21) Kumar, C. S. S. R.; Mohammad, F. Magnetic nanomaterials for hyperthermia-based therapy and controlled drug delivery. *Adv. Drug Delivery Rev.* **2011**, *63*, 789–808.
- (22) Yuan, M.; Wang, Y.; Qin, Y. X. SPIO-Au core—shell nanoparticles for promoting osteogenic differentiation of MC3T3-E1 cells: Concentration-dependence study. *J. Biomed. Mater. Res., Part A* **2017**, *105*, 3350–3359.
- (23) Yuan, M.; Wang, Y.; Qin, Y.-X. Promoting neuroregeneration by applying dynamic magnetic fields to a novel nanomedicine: Superparamagnetic iron oxide (SPIO)-gold nanoparticles bounded with nerve growth factor (NGF). *Nanomedicine* **2018**, *14*, 1337–1347.
- (24) Yuan, M.; Wang, Y.; Qin, Y.-X. Engineered nanomedicine for neuroregeneration: light emitting diode-mediated superparamagnetic iron oxide-gold core-shell nanoparticles functionalized by nerve growth factor. *Nanomedicine* **2019**, *21*, No. 102052.

- (25) Yuan, M.; Wang, Y.; Hwang, D.; Longtin, J. P. Thermocouple-tip-exposing temperature assessment technique for evaluating photo-thermal conversion efficiency of plasmonic nanoparticles at low laser power density. *Rev. Sci. Instrum.* **2019**, *90*, No. 094902.
- (26) Lu, A. H.; Salabas, E. L.; Schüth, F. Magnetic nanoparticles: synthesis, protection, functionalization, and application. *Angew. Chem., Int. Ed.* **2007**, *46*, 1222–1244.
- (27) Laurent, S.; Forge, D.; Port, M.; Roch, A.; Robic, C.; Vander Elst, L.; Muller, R. N. Magnetic iron oxide nanoparticles: synthesis, stabilization, vectorization, physicochemical characterizations, and biological applications. *Chem. Rev.* **2008**, *108*, 2064–2110.
- (28) Yuan, M.; Yan, T.-H.; Li, J.; Xiao, Z.; Fang, Y.; Wang, Y.; Zhou, H.-C.; Pellois, J.-P. Superparamagnetic iron oxide—gold nanoparticles conjugated with porous coordination cages: Towards controlled drug release for non-invasive neuroregeneration. *Nanomedicine* **2021**, *35*, No. 102392.
- (29) Chen, J.; Wang, Y. Personalized dynamic transport of magnetic nanorobots inside the brain vasculature. *Nanotechnology* **2020**, *31*, No. 495706.
- (30) Geng, F.; Xing, J. Z.; Chen, J.; Yang, R.; Hao, Y.; Song, K.; Kong, B. Pegylated glucose gold nanoparticles for improved in-vivo bio-distribution and enhanced radiotherapy on cervical cancer. *J. Biomed. Nanotechnol.* **2014**, *10*, 1205–1216.
- (31) Kong, S. D.; Lee, J.; Ramachandran, S.; Eliceiri, B. P.; Shubayev, V. I.; Lal, R.; Jin, S. Magnetic targeting of nanoparticles across the intact blood—brain barrier. *J. Controlled Release* **2012**, *164*, 49–57.
- (32) Lasagna-Reeves, C.; Gonzalez-Romero, D.; Barria, M. A.; Olmedo, I.; Clos, A.; Ramanujam, V. M. S.; Urayama, A.; Vergara, L.; Kogan, M. J.; Soto, C. Bioaccumulation and toxicity of gold nanoparticles after repeated administration in mice. *Biochem. Biophys. Res. Commun.* **2010**, 393, 649–655.
- (33) Shilo, M.; Motiei, M.; Hana, P.; Popovtzer, R. Transport of nanoparticles through the blood-brain barrier for imaging and therapeutic applications. *Nanoscale* **2014**, *6*, 2146–2152.
- (34) Bondarenko, O.; Saarma, M. Neurotrophic Factors in Parkinson's Disease: Clinical Trials, Open Challenges and Nanoparticle-Mediated Delivery to the Brain. *Front. Cell. Neurosci.* **2021**, *15*, No. 682597.
- (35) Chen, J.; Yuan, M. Y.; Madison, C.; Eitan, S.; Wang, Y. Blood-Brain Barrier Crossing using Magnetic Stimulated Nanoparticles; BioRxiv, 2021.
- (36) Perrault, S. D.; Walkey, C.; Jennings, T.; Fischer, H. C.; Chan, W. C. W. Mediating tumor targeting efficiency of nanoparticles through design. *Nano Lett.* **2009**, *9*, 1909–1915.
- (37) Dante, S.; Petrelli, A.; Petrini, E. M.; Marotta, R.; Maccione, A.; Alabastri, A.; Quarta, A.; De Donato, F.; Ravasenga, T.; Sathya, A.; et al. Selective targeting of neurons with inorganic nanoparticles: revealing the crucial role of nanoparticle surface charge. *ACS Nano* **2017**, *11*, 6630–6640.
- (38) Arvizo, R. R.; Miranda, O. R.; Thompson, M. A.; Pabelick, C. M.; Bhattacharya, R.; Robertson, J. D.; Rotello, V. M.; Prakash, Y. S.; Mukherjee, P. Effect of nanoparticle surface charge at the plasma membrane and beyond. *Nano Lett.* **2010**, *10*, 2543–2548.
- (39) Gaiduk, A.; Ruijgrok, P. V.; Yorulmaz, M.; Orrit, M. Making gold nanoparticles fluorescent for simultaneous absorption and fluorescence detection on the single particle level. *Phys. Chem. Chem. Phys.* **2011**, *13*, 149–153.
- (40) Bancroft, E. A.; Srinivasan, R. Quantifying Spontaneous Ca²⁺ Fluxes and their Downstream Effects in Primary Mouse Midbrain Neurons. *J. Visualized Exp.* **2020**, No. e61481.
- (41) Zarate, S. M.; Pandey, G.; Chilukuri, S.; Garcia, J. A.; Cude, B.; Storey, S.; Salem, N. A.; Bancroft, E. A.; Hook, M.; Srinivasan, R. Cytisine is neuroprotective in female but not male 6-hydroxydopamine lesioned parkinsonian mice and acts in combination with 17- β -estradiol to inhibit apoptotic endoplasmic reticulum stress in dopaminergic neurons. *J. Neurochem.* **2021**, *157*, 710–726.
- (42) Henley, B. M.; Cohen, B. N.; Kim, C. H.; Gold, H. D.; Srinivasan, R.; McKinney, S.; Deshpande, P.; Lester, H. A. Reliable Identification of Living Dopaminergic Neurons in Midbrain Cultures

- Using RNA Sequencing and TH-promoter-driven eGFP Expression. J. Visualized Exp. 2017, No. e54981.
- (43) Davenport, B.; Li, Y.; Heizer, J. W.; Schmitz, C.; Perraud, A.-L. Signature channels of excitability no more: L-type channels in immune cells. *Front. Immunol.* **2015**, *6*, No. 375.
- (44) Laryushkin, D. P.; Maiorov, S. A.; Zinchenko, V. P.; Gaidin, S. G.; Kosenkov, A. M. Role of L-Type Voltage-Gated Calcium Channels in Epileptiform Activity of Neurons. *Int. J. Mol. Sci.* **2021**, 22, No. 10342.
- (45) Tang, L.; El-Din, T. M. G.; Lenaeus, M. J.; Zheng, N.; Catterall, W. A. Structural basis for diltiazem block of a voltage-gated Ca²⁺ channel. *Mol. Pharmacol.* **2019**, *96*, 485–492.
- (46) Achermann, P.; Rusterholz, T.; Dürr, R.; König, T.; Tarokh, L. Global field synchronization reveals rapid eye movement sleep as most synchronized brain state in the human EEG. *R. Soc. Open Sci.* **2016**, *3*, No. 160201.
- (47) König, T.; Lehmann, D.; Saito, N.; Kuginuki, T.; Kinoshita, T.; Koukkou, M. Decreased functional connectivity of EEG theta-frequency activity in first-episode, neuroleptic-naive patients with schizophrenia: preliminary results. *Schizophr. Res.* **2001**, *50*, 55–60.
- (48) Zhang, S.; Qi, Y.; Yang, H.; Gong, M.; Zhang, D.; Zou, L. Optimization of the composition of bimetallic core/shell Fe₂O₃/Au nanoparticles for MRI/CT dual-mode imaging. *J. Nanopart. Res.* **2013**, *15*, No. 2023.
- (49) Li, J.; Sun, J.; Chen, T.; Li, X. Towards a better understanding of the effects of the magnetic nanoparticles size and magnetic field on cellular endocytosis. *J. Phys. D: Appl. Phys.* **2020**, *53*, No. 175401.
- (50) Zheng, Y.; Dou, J.-r.; Gao, Y.; Dong, L.; Li, G. Effects of 15 Hz square wave magnetic fields on the voltage-gated sodium and potassium channels in prefrontal cortex pyramidal neurons. *Int. J. Radiat. Biol.* **2017**, 93, 449–455.
- (51) Bancroft, E. A.; Pandey, G.; Zarate, S. M.; Srinivasan, R. Extracellular S100B Alters Spontaneous Ca²⁺ Fluxes in Dopaminergic Neurons via L-Type Voltage Gated Calcium Channels: Implications for Parkinson's Disease; bioRxiv, 2021.
- (52) Georgas, E.; Yuan, M.; Wang, Y.; Qin, Y.-X. In Remote Regulation of Ca2+ Activities and Action Potential by Dynamic Magnetic Field Stimulated Superparamagnetic Iron Oxide Gold Core Shell Nanoparticles, Cellular and Molecular Bioengineering Conference (2022 CMBE); Indian Wells: CA, USA, 2022.
- (53) Bai, Q.; He, J.; Qiu, J.; Wang, Y.; Wang, S.; Xiu, Y.; Yu, C. Rotenone induces KATP channel opening in PC12 cells in association with the expression of tyrosine hydroxylase. *Oncol. Rep.* **2012**, *28*, 1376–1384.
- (54) Brignani, S.; Pasterkamp, R. J. Neuronal subset-specific migration and axonal wiring mechanisms in the developing midbrain dopamine system. *Front. Neuroanat.* **2017**, *11*, No. 55.
- (55) Voigt, T.; Baier, H.; de Lima, A. D. Synchronization of neuronal activity promotes survival of individual rat neocortical neurons in early development. *Eur. J. Neurosci.* **1997**, *9*, 990–999.
- (56) Hardingham, G. E.; Fukunaga, Y.; Bading, H. Extrasynaptic NMDARs oppose synaptic NMDARs by triggering CREB shut-off and cell death pathways. *Nat. Neurosci.* **2002**, *S*, 405–414.
- (57) Martin, H. G. S.; Wang, Y. T. Blocking the deadly effects of the NMDA receptor in stroke. *Cell* **2010**, *140*, 174–176.
- (58) Hardingham, G. E.; Bading, H. The Yin and Yang of NMDA receptor signalling. *Trends Neurosci.* **2003**, *26*, 81–89.
- (59) Lee, S.; Liu, A.; Wang, Z. J.; McKeown, M. J. Abnormal phase coupling in Parkinson's disease and normalization effects of subthreshold vestibular stimulation. *Front. Hum. Neurosci.* **2019**, *13*, No. 118.
- (60) Jalili, M.; Barzegaran, E.; Knyazeva, M. G. Synchronization of EEG: bivariate and multivariate measures. *IEEE Trans. Neural Syst. Rehabil. Eng.* **2013**, 22, 212–221.

